ELSEVIER

Polymer 43 (2002) 5197–5207

polymer

www.elsevier.com/locate/polymer

Real time SAXS/stress–strain studies of thermoplastic polyurethanes at large strains

D.J. Blundell[a], G. Eeckhaut[b], W. Fuller[a], A. Mahendrasingam[a,*], C. Martin[a]

[a]*Department of Physics, School of Chemistry and Physics, University of Keele, Keele, Staffordshire ST5 5BG, UK*
[b]*Huntsman Polyurethanes R&D, Everslaan 45, B-3078 Everberg, Belgium*

Received 8 March 2002; received in revised form 5 June 2002; accepted 10 June 2002

Abstract

Simultaneous small angle X-ray scattering (SAXS) and force measurements have been recorded during tensile deformation of two contrasting polyurethane elastomers. The elastomers comprise the same hard and soft chemical segments; in Sample A, the length of the hard blocks is randomised while in Sample B the hard blocks are monodisperse. During deformation of Sample A, the SAXS halo from the mesophase structure deforms to an ellipse with intensification on the meridian. In Sample B, the halo transforms into a four point pattern. The ellipse patterns of A are interpreted in terms of a model based on particles located on a statistical lattice which is subjected to an affine deformation scheme. According to this model, the SAXS patterns of A are consistent with the hard phase regions behaving as embedded particles which separate from each other in an affine manner and which are not impeded by interconnections during the mechanical yield process. In B, the interconnection of the hard phase prevents affine deformation of the structure and involves the formation of a four point 'lattice' structure which then subsequently deforms in an affine manner. The differences in behaviour are linked with the segment sequencing which result in the phase regions of Sample A having a lower volume fraction and are consistent with variation in applied stress.

Keywords: Small angle X-ray scattering; Polyurethanes; Stress–strain

1. Introduction

Poly(urethane) elastomers are synthesised in the simultaneous condensation co-polymerisation of three components: a polyol—a generic term for a hydroxyl terminated poly(ether), poly(ester) or poly(alkyl) chain of intermediate molecular weight (1000–6000 g/mol); a diisocyanate; and a chain extender. The result is an $(AB)_n$ type segmented chain architecture with relatively short but numerous A and B segments. The A segments, which are built from alternating sequences of chain extender and diisocyanate molecules, are referred to as 'hard' segments. The B segments are known as 'soft' segments and originate from the polyol. It has been established [1–3] that at a certain point in time the growing hard segments phase separate in a spinodal mechanism from the soft segments. This results in the formation of a mesophase structured polymer containing glassy, hard domains and rubbery, soft domains where the respective glass transition temperatures are above and below the normal service temperatures of the polymer. When all the components of the polyurethane are difunctional, the resulting polymer becomes thermoplastic allowing the material to be melt or solvent processed. The exact nature of the final morphology is uncertain and depends on the fabrication route as well as the molecular formulation [4] and involves ripening of the spinodal driven phase separation process. The size scale of the density fluctuations of the mesophase morphology is closely linked to the characteristic molecular dimensions of the hard and soft segments and is of the order of 10 nm, thus allowing the morphology to be monitored by small angle X-ray scattering (SAXS).

Despite their versatility for a wide range of uses, applications of thermoplastic polyurethanes are still limited by their relatively high mechanical hysteresis compared with other elastomers. This hysteresis and the associated mechanical loss processes can be partly attributed to the breakdown and reformation of the mesophase morphology during mechanical cycling. Over the years there has been a

* Corresponding author. Tel.: +44-1782-583312; fax: +44-1782-583320.
E-mail address: a.mahendrasingam@keele.ac.uk (A. Mahendrasingam).

0032-3861/01/$ - see front matter
PII: S0032-3861(02)00386-5

continuing interest in the impact of mechanical deformation on the mesophase structure in segmented linear polyurethanes. Ryan et al. [5] reviewed the general morphology principles in urethane elastomers derived from X-ray and other methods. Koberstein in 1983 discussed the details of the domain structure and the boundary thickness between the hard and soft domains from SAXS and DSC measurements [6,7]. The earliest papers on PU deformation focused on the modulus versus temperature behaviour and hinted that the enhanced modulus could be ascribed to the glassy state of the phase separated hard blocks acting as 'fillers' for the elastomeric blocks [8–11]. Very early on, the orientation behaviour of urethane and urea block copolymers under uniaxial extension was studied by X-ray diffraction and infrared dichroism. Bonart [12,13] was amongst the first to identify the orientation of the periodic microphase structure under tensile deformation. Later Desper et al. [14] using data collected on Kratky and pinhole cameras, identified different modes of deformation depending upon the shape and structural integrity of the hard block domains in which the mesophase structure deforms either by local shearing or local tensile deformation of the soft segments. Structure–property relations in moulded plaques of flexible polyurethane foams were investigated by Moreland and Wilkes [15] by IR dichroism. They identified a two-step orientation–elongation mechanism. The region below 50% elongation was associated with low hysteresis in which lamella-like hard domains aligned along the strain direction in a more or less reversible manner. Above 50% elongation, the hard domains are disrupted, with individual hard segments being pulled away from the hard domains. Later the importance of hard segment length distribution was recognised. Eisenbach et al. [16,17] synthesised and characterised polyurethane elastomers with monodisperse hard segment length distributions. Also Musselman et al. [18] synthesised and characterised with SAXS and DSC a series of poly(urethaneurea) elastomers derived from toluene diisocyanates prepolymers. Via this specific route, elastomers with better defined, less polydisperse hard segment lengths were obtained. These elastomers had higher tensile moduli and improved mechanical properties compared with corresponding conventional PU elastomers with polydisperse hard segment length distributions [19].

As with much of these previous studies, the present paper shares the aim of providing insight into property improvement by understanding how the morphology and its evolution is controlled by the chemical building blocks of the material and by deformation processes. The paper describes experiments on thermoplastic polyurethane elastomers involving the simultaneous measurement of the two-dimensional (2D) SAXS patterns and the stress during tensile deformation, using synchrotron X-ray sources. This study was carried out on two contrasting polyurethanes that had been synthesised from the same components but with different distributions of hard and soft block lengths. These materials provide a contrast both between the initial morphologies and between the nature of the evolution of the morphologies during the mechanical deformation cycle, thus giving an insight into the mechanisms contributing to mechanical loss. In the experiments, the samples have been subjected to a repeated extension and retraction cycle beyond the yield point. This paper is primarily concerned with the initial extension and with analysing changes in the mesophase morphology that occur during yield (draw ratio $\sim$1.1) and during subsequent extension up to draw ratios $>$2. Further work is in progress to analyse the structural changes that are associated with hysteresis during the repeated extension and retraction cycle.

Several analytical approaches are being used on the data to elucidate the nature of both the starting morphologies and how the morphologies change during deformation. Past studies of mesophase morphology have often interpreted SAXS in terms of lamellar domains as a conceptual aid to understand the data [14,18]. However, the approach used in this paper is to avoid any presumptions based on such specific structural models. The analyses in this paper combine an evaluation of generally applicable parameters with a novel empirical approach based on the affine deformation concept [20].

2. Experimental

2.1. Samples

The two polyurethane samples used in this study were synthesised from the same building blocks. The basic soft block units are derived from Dupont 'Terethane1000' which is a α,ω-dihydroxy poly(tetrahydrofurane) of nominal molecular weight 1000 g/mol^{-1}; GPC analysis indicates that $M_w/M_n = 1.4$. The hard segments consisted of mixtures of toluene 2,4-diisocyanate (TDI), 4,4′-methylenediphenyleneisocyanate (MDI) and ethanolamine (EA) in a molar ratio = 2:1:2. For both samples, the relative proportions of components were equivalent to a hard segment content of $\sim$42 wt% which is equivalent to $\sim$36 vol%.

Sample A was synthesised in a one shot solvent process in dried dimethylacetamide. All chemicals were at once mixed at the same time in the solvent to encourage a randomised reaction of components so as to produce a polydispersity in the lengths of both the hard and soft blocks.

Sample B was synthesised in a series of systematic steps so as to form monodispersed alternating hard blocks of TDI–EA–MDI–EA–TDI and soft blocks of one poly(THF) diol unit. The structure of the hard segments is shown in Scheme 1 and has a molecular weight of 720 g/mol. This structure can also be regarded as the statistical average structure of the polydisperse hard blocks in Sample A.

The polymers were cast from a solution with

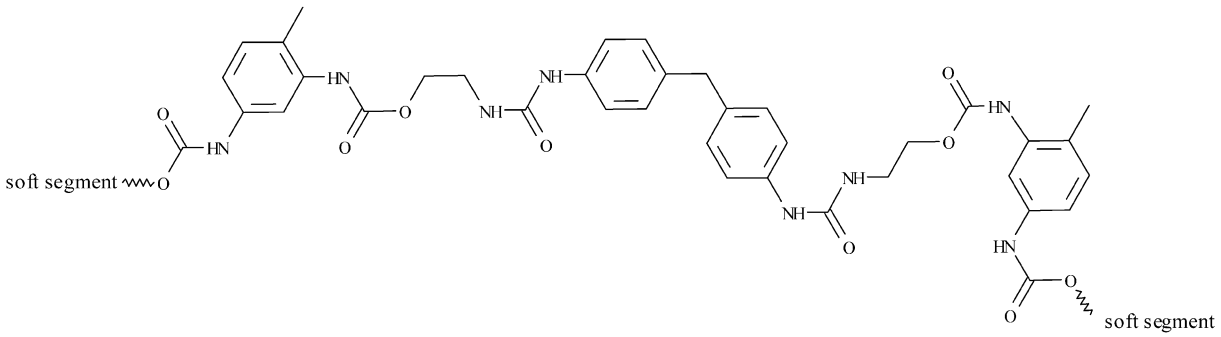

Scheme 1.

dimethylacetamide into 0.7 mm thick sheets, dried and then post annealed at 80 °C for 24 h.

2.2. Static SAXS of undeformed samples

One-dimensional (1D) SAXS data from the isotropic, undeformed samples were collected on beamline 2.1 at the Daresbury SRS using a quadrant detector. The data was analysed using established procedures [21] assuming that the tail at large values of the scattering vector q can be approximated by

$$\underset{q\to\infty}{I} = \frac{K_p}{q^4}\exp\left(-\frac{E^2q^2}{12}\right) + B \quad (1)$$

where B is the background contribution from density fluctuations and is assumed to be constant over the measured q-range, K_p the Porod constant that characterises the asymptotic behaviour at high q and E is a measure of the thickness of the interface between mesophase regions [22].

The intensity was calibrated by reference to a secondary standard Lupolen sample that had been previously calibrated at the Oak Ridge National Laboratory [23].

After subtraction of the background B, the intensity data was used to derive the Invariant quantity Inv:

$$\mathrm{Inv} = \frac{1}{2\pi^2}\int_0^\infty I(q)q^2\,\mathrm{d}q \quad (2)$$

This information was used to derive the Porod chord length parameter, l_p [24]

$$l_p = \frac{8\pi\mathrm{Inv}}{K_p} \quad (3)$$

2.3. Real time SAXS experiments

The real time deformation experiments were carried out using a purpose designed stretching camera [25,26] that had been constructed in the Keele Physics Department workshops. The jaws of the camera were connected to separate stepping motors that could be programmed to a predetermined deformation cycle. For some of the present experiments, the camera was modified by incorporating a 100 N load cell into one of the jaw assemblies to enable the stretching force to be monitored. The camera had a viewing port that enabled the deformation of the samples to be recorded on a synchronised video signal.

Ten-millimeter wide strips were cut from the polyurethane sheets and mounted in the jaws of the camera with an effective gauge length of around 17 mm. The samples were subjected to a pre-programmed linear, loading cycle during which SAXS patterns were recorded with sequential frames every 3.2 s. This is equivalent to a strain rate of around 0.01 s^{-1}. Although all the samples were subjected to the same nominal deformation cycle, there were small differences in the clamping which resulted in some variation in the actual draw ratios achieved in each experiment. Therefore, 1 mm separated stripes were drawn on the sample at right angles to the draw axis to enable the actual strain to be deduced from the video image.

The camera assembly was used to record two series of experiments using synchrotron X-ray sources. The first series was carried out at the Daresbury SRS with a wavelength of 0.14 nm using beamline 16.1 with the RAPID area detector and with the load cell assembly installed. The second series used the ID2A SAXS beamline at the ESRF in Grenoble using the CCD detector and a wavelength of 0.0995 nm. There were differences in the configuration and beam monitoring facilities between the SRS and the ESRF. These differences had advantages and disadvantages for particular analyses. There was consistency between experiments in the SAXS patterns at each level of draw ratio so the most favourable data set was therefore chosen for each analysis.

2.4. Analysis of 2D patterns

After correcting for detector characteristics and subtracting the instrumental background, the data sets were analysed with macro routines to determine the loci and peak intensities of the diffraction halos.

In order to evaluate the invariant integrals from the 2D patterns, axial symmetry was assumed. The calculations were based on one of the quadrants that did not contain spurious data from the beam stop support. Accordingly the

invariant integral will be proportional to

$$\text{Inv} \propto 4\pi \int_0^{\infty} \left(\int_0^{\pi/2} (I_{\text{obs}}(\phi, q) - B)\sin(\phi)\mathrm{d}\phi \right) q^2 \, \mathrm{d}q \qquad (4)$$

where I_{obs} is the observed intensity which is a function of the scattering vector q and azimuthal angle ϕ and B is the sample background scatter due to random density fluctuations and for convenience it is taken to be a constant.

The internal integral in ϕ was evaluated as a first step to reduce the relationship to the form

$$\text{Inv} \propto 4\pi \int_0^{\infty} (I_q(q) - B)q^2 \, \mathrm{d}q \qquad (5)$$

For convenience it was assumed that Porod's Law was applicable so that for large values of q

$$\lim_{q \to \infty} (I_q - B) = \frac{A}{q^4} \qquad (6)$$

where A is a constant.

The constants A and B were evaluated by curve fitting in the high q region starting at a q value at twice that of the diffraction peak. The level of signal to noise was not sufficient to enable the high q data to be analysed for the effects of a finite interface between phases.

3. Results

As indicated above in Section 2, the SAXS experiments were carried out at both the SRS and ESRF using different beamline configurations, resulting in data sets covering different ranges of q. The results and analyses reported and discussed here are selected from the data sets that are optimum for each type of analysis.

The static, 1D SAXS data of the undeformed samples are shown in Fig. 1. There are clear differences in the periodicity and in the degree of order between the samples, with Sample A having the larger periodicity and sharper diffraction peak. The higher degree of apparent order in Sample A could be a consequence of a greater degree of ripening of the structural organisation from the spinodal decomposition process.

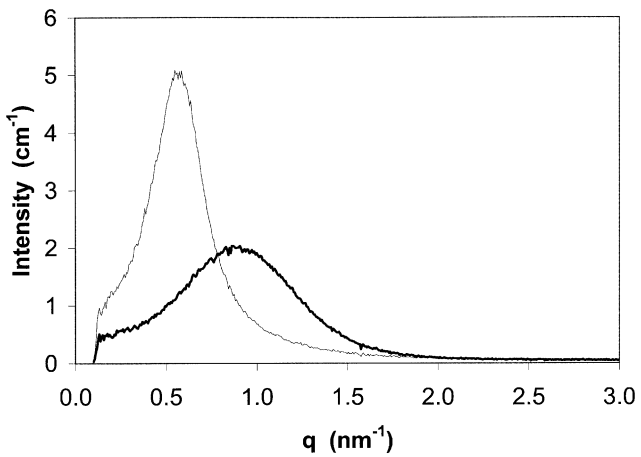

Fig. 1. Static 1D SAXS of undeformed elastomer samples: fine line = Sample A, bold line = Sample B.

Table 1 summarises some of the parameters derived from an analysis of these data. There is a significant difference in the invariant integral which is expected to be due to differences in the volume fraction and composition of the hard and soft phases. The interface thickness between the mesophase regions is relatively narrow and indicates that reasonable short range ripening has occurred.

The variation in tensile force recorded during deformation in both samples during the SRS experiments are shown in Fig. 2. In order to aid comparison with the SAXS data, the force is plotted against the equivalent SAXS frame number, where each frame is equivalent to 3.2 s. The draw ratio attained in these experiments at frame 55 is 2.3:1. Both samples show very similar behaviour in the shape of the force variation with a yield process at around draw ratio 1.1 corresponding to frame 5. This is followed by a more linear response starting at around the point corresponding to a draw ratio of about 1.25, corresponding to frame 10. However, as shown in the more detailed plot in Fig. 3, the initial slopes are significantly different and are equivalent to moduli of 83 and 130 MPa for Samples A and B, respectively.

Selected SAXS frames from these SRS experiment are shown in Figs. 4 and 5. There is a very marked difference between the two samples in the way the SAXS patterns develop during the loading cycle. The differences resemble those observed between the different formulations of polyurethanes studied by Desper et al. [14].

During tensile loading, the diffraction halo of Sample A intensifies on the meridian and becomes progressively elliptical in shape. Within experimental error, the diffraction halos for all of the patterns of Sample A follow the locus of an ellipse (i.e. $x^2/a^2 + z^2/b^2 = 1$). This can be confirmed from plots of x^2 versus z^2 as in the examples in Fig. 6, where z is in the vertical draw direction and x is in the lateral direction.

The behaviour of Sample B is distinctly different.

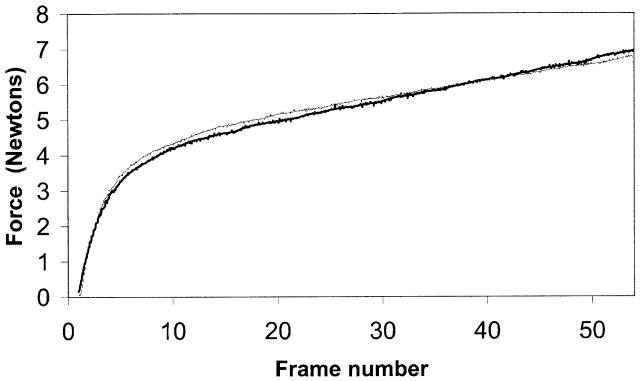

Fig. 2. Variation in tensile force from SRS experiment: bold line = Sample A, fine line = Sample B. Each frame corresponds to a time interval of 3.2 s.

Table 1
Summary of parameters derived from static, 1D SAXS data

Parameters	Sample A	Sample B
Peak Bragg spacing (nm)	11	7.2
Invariant (nm^{-4}) from Eq. (2)	6.8×10^{-9}	9.3×10^{-9}
Interface thickness, (E, nm) from Eq. (1)	0.3	0.5
Porod chord length, (l_p, nm) from Eq. (3)	2.6	3.6
Mean chord length of hard phase (l_H, nm) from Eq. (9)	4.1	5.6

Although a slight ellipticity develops during the first extension, the main effect is an off-axis intensification producing a 'four point' pattern in which there is a systematic movement in the position of the four points with the degree of sample deformation.

The results of the invariant integration from the ESRF experiments, which are shown along with the applied draw ratio in Fig. 7, also reveal differences in behaviour. In the case of Sample A, there is a decrease with increasing deformation whereas Sample B shows a small increase.

4. Discussion

4.1. Affine deformation in Sample A

An elliptical locus can be derived from a circle by an affine deformation; i.e. a deformation in which all x and z coordinates are systematically multiplied by constants fx and fz, respectively. It is therefore of interest to enquire whether the elliptical shapes of the halos for Sample A can be directly linked with an affine deformation of the two-phase structure in the specimen. Assuming that polyurethane elastomers deform at close to constant volume, then during uniaxial tensile deformation of draw ratio λ the length of the sample will change by λ while the lateral dimensions will change by a factor of $1/\sqrt{\lambda}$. If the two-phase microstructure follows an affine deformation scheme related

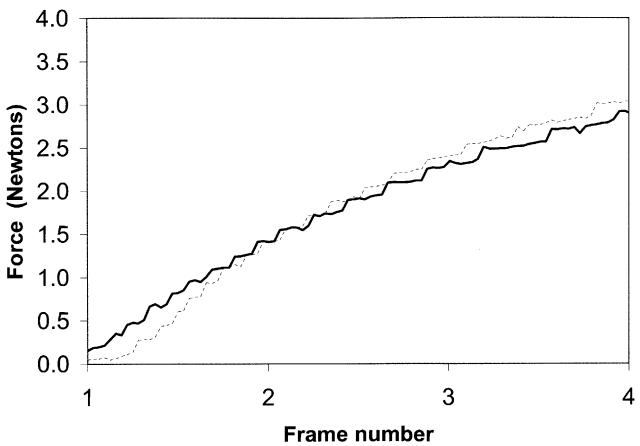

Fig. 3. Variation in tensile force from SRS experiment during initial deformation: bold line = Sample A, fine line = Sample B. Each frame corresponds to a time interval of 3.2 s.

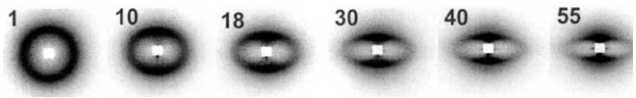

Fig. 4. Selected SAXS patterns from the SRS data of Sample A for frames 1, 10, 18, 30, 40 and 55.

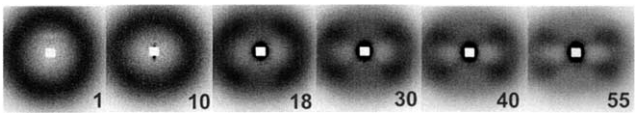

Fig. 5. Selected SAXS patterns from the SRS data of Sample B for frames 1, 10, 18, 30, 40 and 55.

to the overall sample shape then the x and z coordinates of a vector between any two structural elements in real space will be modified by the same factors. In such a situation, the corresponding intensity function in reciprocal space will also deform affinely but with factors that are the inverse of those in real space. Thus x and z coordinates of vectors in reciprocal space will be changed by factors of $fx = \sqrt{\lambda}$ and $fz = 1/\lambda$, respectively. If the circular halo of the undeformed specimen has a radius x_0 ($= z_0$) then $x/x_0 = \sqrt{\lambda}$ and $z/z_0 = 1/\lambda$. This hypothetical situation can be partially tested on the experimental data by plotting the two parameters $(x/x_0)^2$ and z_0/z versus λ. As shown in Fig. 8, the data points closely follow the value of λ up to a draw ratio of around 1.25. Beyond this the data points diverge and indicate a larger degree of ellipticity than that predicted for affine deformation. The point of the divergence corresponds

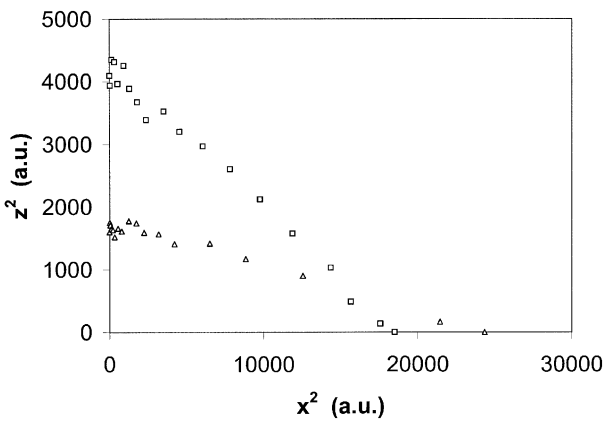

Fig. 6. Plots of loci of intensity maxima around the elliptical patterns for SRS data of Sample A: □ = frame 20; △ = frame 55.

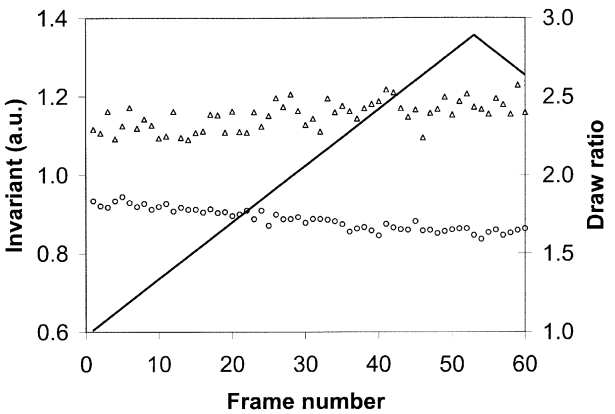

Fig. 7. Variation of invariant integral (Eq. (4)) from ESRF experiment: □ = Sample A; △ = Sample B; full line = draw ratio. Each frame corresponds to a time interval of 3.2 s.

to the onset of the more linear strain response in Fig. 2 and suggests there may be a link with the way in which the microstructure deforms.

Up until this point there is therefore an indication that the main features of the microstructure are deforming in a way that is related to an affine scheme. However, one needs to examine the implications of this for the nature of the phase morphology. In a true affine deformation, every feature and shape of the phase morphology would need to deform in an affine manner. In an associated way all the features of the corresponding intensity function in reciprocal space would undergo a reciprocal affine deformation. Thus, a circular diffraction halo with uniform intensity would deform to an oblate ellipse that also had a uniform intensity. This is clearly not the case for the observed elliptical halos in Fig. 4 where there is a very marked intensification on the meridian. One can conclude therefore that, despite the ellipticity being consistent with affine deformation of the periodicities within the structure, the shapes of the microphases are not themselves following the true affine scheme.

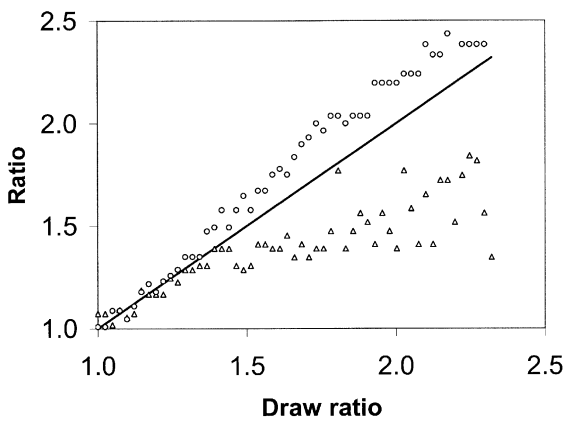

Fig. 8. Plots versus draw ratio for Sample A from SRS experiment, showing the relationship with the affine deformation scheme: □ = x^2/x_0^2; △ = z_0/z; full line = predicted affine behaviour.

4.2. Statistical particulate model

The above conclusion is not surprising if one bears in mind the composition of the polyurethane elastomer. It is unrealistic to expect the above true affine model to hold since the hard and soft phases have quite different mechanical properties. The hard microphase regions will resist changes in shape while the soft phase will tend to change shape to accommodate the hard phase. When the hard phase is in the minority, as in this specimen, the degree of connectivity of the hard phase will be reduced. One would therefore expect that the larger concentrations of hard phase will be more able to retain their original shapes during the deformation of the macroscopic sample. It is therefore of interest to consider a modified affine model in which the hard microphase regions can effectively be represented by separated particulate inclusions embedded in a continuous soft phase and to ignore regions of connectivity between the hard phase concentrations. Assume therefore that during deformation, the relative positions of the hard phase particles with respect to each other move affinely but the shapes of the particles remain unchanged. In this model the particles represent the main concentrations of hard phase and will vary in shape and size. The contrast between true affine and the modified affine deformation is shown in Fig. 9 for the simplified case of spherical particles.

The diffraction halo will result from the interference between waves scattered from this statistical arrangement of particles. Making the analogy with standard crystallography, one can consider the particles to be located on statistical lattice points. The observed intensity along any given scattering direction will therefore be the product of a particle function (PF) and a lattice function (LF). In the undeformed, isotropic state, LF will be centrosymmetric. During deformation the statistical lattice points will move according to the affine scheme. The LF will then vary with direction in such a way that the profile of LF will deform in an affine manner that is the reciprocal of the deformation of the real-space, statistical lattice. In contrast, PF will be isotropic and will remain unchanged during deformation. Accordingly, the peak intensity of the observed intensity

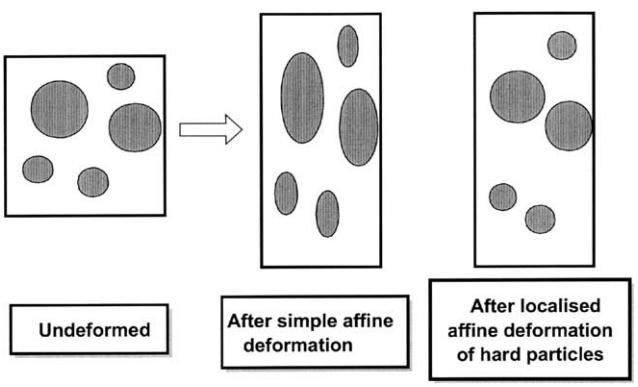

Fig. 9. Illustration of particulate model showing differences between pure affine deformation and modified affine deformation.

halo in any particular direction will be determined by the value of PF at the peak scattering vector of LF. This is analogous to the crystallography of perfect crystals where the intensity of each discrete crystalline reflection is due to the sampling of the structure factor of the unit cell at each reciprocal lattice point. As an illustrative example of a statistical lattice consider the simple case in which the periodic regularity in any particular direction is represented by a 1D lattice factor (LF) in the form of a Zernike–Prins term [27]

$$\mathrm{LF} = \frac{(1 - |F|^2)}{(1 - 2|F|\cos(qd) + |F|^2)} \tag{7}$$

where $F = \exp(-q^2 g^2 d^2/2)$, and d the periodic repeat and g is the fractional deviation of the distribution of projected distances between scatterers.

Also for simplicity, assume that the hard phase inclusions can be represented by identical spheres of radius R with a particle scattering factor [28]

$$\mathrm{PF} = \frac{9(\sin(Rq) - Rq\cos(Rq))^2}{(Rq)^6} \tag{8}$$

The predicted intensity is the product of the LF and PF terms. During deformation, the periodic distance d will vary with direction according to an affine scheme causing the q-radius at the peak of the halo to vary with direction in a reciprocal way. The intensity around the halo will be determined by the value of PF at the q value of the peak in that direction. Fig. 10 shows a predicted SAXS pattern expected for an affine deformed sample for the particular case where the sphere radius is 0.4 of the average periodic repeat, the deviation g is 0.25 of the periodic repeat and the draw ratio $\lambda = 1.4$.

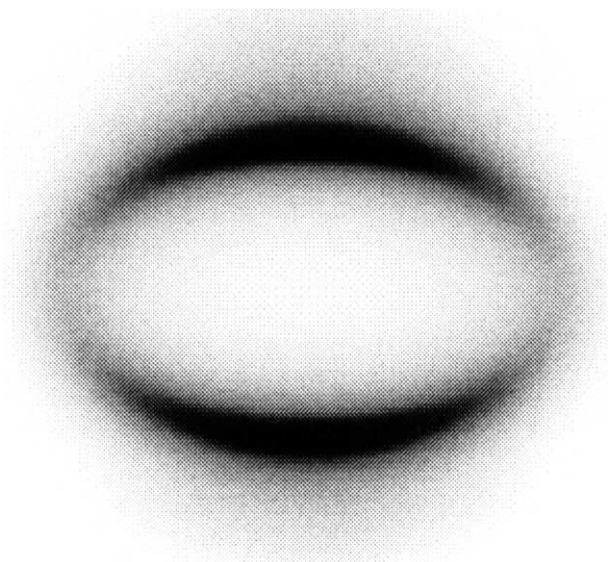

Fig. 10. Example of a predicted SAXS pattern for the model of spherical particles located on a deformed statistical lattice calculated from Eqs. (7) and (8), assuming $R = 0.4d$, $g = 0.25$ and $\lambda = 1.4$.

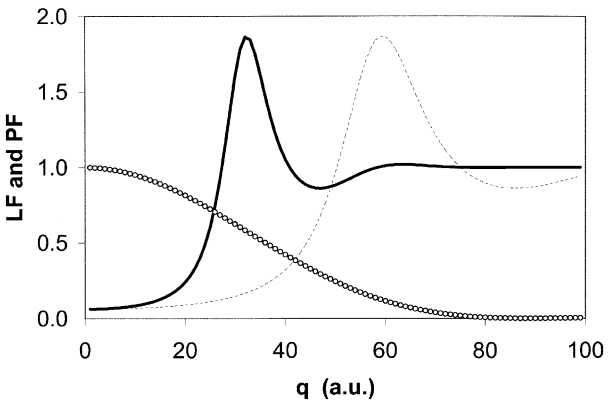

Fig. 11. Contributions of LF (Eq. (7)) and PF (Eq. (8)) for predicted pattern in Fig. 10: solid line = LF on meridian; dashed line = LF on equator; ○ = PF.

Fig. 11 shows how the LF and PF contribute to the intensity of the elliptical halo along the meridian and equator axes.

Fig. 10 reasonably reproduces the features of the observed SAXS patterns of Sample A. If one accepts this approach for interpreting the experimental patterns then one can consider the corollary of the argument that the intensity variation around the ellipse gives direct information of the structure factor of the particles located on the statistical lattice. (Interestingly, the exact form of LF does not need to be known providing the positions of the statistical lattice points deform affinely.) Fig. 12 shows the variation of intensity as a function of the square of the radii for frame 10, plotted on a log scale. This plot is equivalent to a Guinier plot for the scattering particles [29] plotted between the limits of the major and minor axes of the elliptical halo. A linear fit to these points indicates that the effective radius of gyration of the particles is 2.7 nm. Identical spherical particles with this radius of gyration would have a diameter of 6.9 nm. Bearing in mind the dispersity in size expected for the equivalent particles that represent the hard phase concentrations in this model, this derived particle dimension is sensibly consistent with the 11 nm periodic repeat of the undeformed diffraction halo and with the hard segment volume fraction derived from the chemical composition. It is also consistent with the derived chord length parameter, l_p. If the volume fraction of the hard phase is ϕ, then mean chord intercept length through the hard phase regions will be

$$l_H = \frac{l_p}{1 - \phi} \tag{9}$$

As indicated in Table 1, if the hard phase occupies the nominal volume fraction of all the hard segments (= 0.36), then l_H is 4.1 nm. If one assumes for simplicity that the hard phase regions can be represented by identical spheres, then the equivalent diameter of the spheres [24] will be $1.5 \times 4.1 = 6.15$ nm. This is in good agreement with the above estimate derived from Fig. 12 and substantiates the

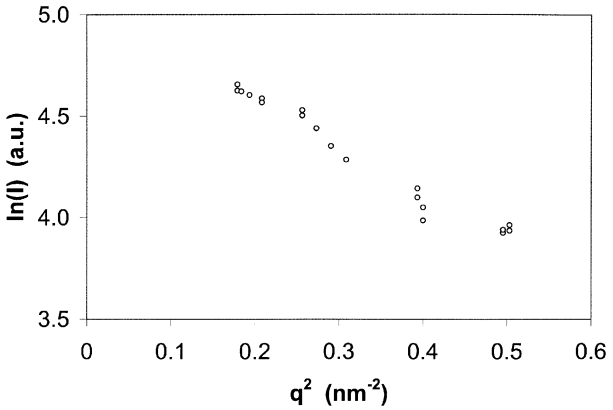

Fig. 12. Variation of peak intensity versus ellipse radius for frame 15 of Sample A, plotted in the form of a Guinier plot.

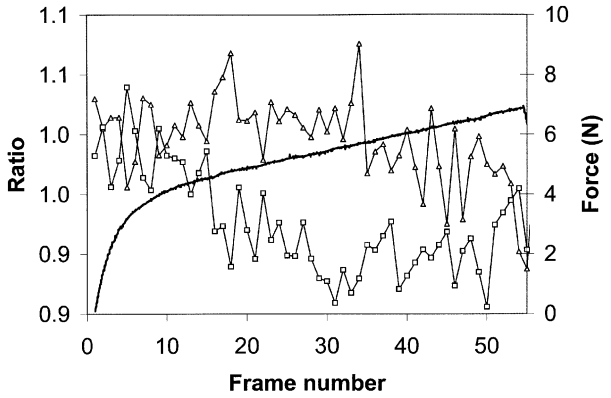

Fig. 13. Plots for Sample A of fictive parameter ratios defined by Eqs. (12) and (13): △ = R_d; □ = R_z; continuous line = force variation. Each frame corresponds to a time interval of 3.2 s.

concept of the particulate model. It is of interest to note that the intensification on the meridian can be accounted for in this particulate model without needing to specify hard phase domains with lamella-like shape, as in the previous study by Desper et al. [14].

4.3. Deviations from particulate model

The deviation of the plots in Fig. 8 beyond a draw ratio of around 1.25 indicates a change in the relative movement of the phase morphology away from affine deformation. However, the fact that the halo retains an elliptical shape also implies that the deformation of the morphology must continue to retain some degree of affine character. The behaviour at higher draw ratios can be explored by considering the apparent affine character in terms of two fictive parameters which can be defined directly from the observed ellipticity. For major and minor radii x and z, one can define a fictive draw ratio λ_f and a fictive radius z_f that can be associated with the circular halo of a fictive undeformed morphology. From the expectations of affine deformation already discussed above

$$\lambda_f = \frac{z_f}{z} = \left(\frac{x}{x_f}\right)^2 \tag{10}$$

hence since $x_f = z_f$

$$\lambda_f = \left(\frac{x}{z}\right)^{2/3} \text{ and } z_f = z^{1/3}x^{2/3} \tag{11}$$

The deviation from actual affine deformation can then be investigated from the ratios of the fictive to the actual parameters

$$R_d = \frac{\lambda_f}{\lambda} \tag{12}$$

and

$$R_z = \frac{z_f}{z_0} \tag{13}$$

Fig. 13 shows a plot of these ratios together with the variation in the applied stress. Up to frame 10 covering the region just beyond the yield process, the ratios are close to unity showing that the morphology is following an affine deformation scheme, as already shown by Fig. 8. Beyond this point and despite the deviation shown in Fig. 8, R_d continues close to unity showing that the fictive draw ratio continues to follow the applied draw ratio. The main effect beyond frame 10 is in R_z, indicating a reduction in z_f. This behaviour can be rationalised, as follows, in terms of the above particulate model. The hard phase regions, which are represented in the model by the particles, will be of varying size and stability. The smaller, less stable regions could be eliminated under the influence of the higher localised stress experienced at higher draw ratios. This would increase the mean distance between the remaining particles and hence move the position of correlation peaks to a lower q, thus reducing z_f. However the remaining, more stable particles would continue to separate from each other in an affine manner that is consistent with the applied draw ratio.

4.4. Deformation of four point pattern in Sample B

The development of the four point pattern in Sample B indicates the formation of a more structured relationship between the hard phase regions during the deformation process. The four point feature first becomes resolvable at a draw ratio of around 1.12 in the region of the yield process in the stress–strain curves. This indicates that the yield is closely associated with the formation of a new structural arrangement that facilitates the compliance of the material. In order to characterise these more complex patterns, measurements were therefore made as in Fig. 14 of the coordinates p_x and p_y of the four point maxima as well as the ellipticity, defined by the major and minor axes.

This analysis was carried out on a data set from the ESRF where the q range was more favourable for this measurement. A plot of the two ellipticity parameters, $(x/x_0)^2$ and z_0/z, versus λ is shown in Fig. 15. Unlike the case of Sample A, the parameters fail to follow the affine deformation

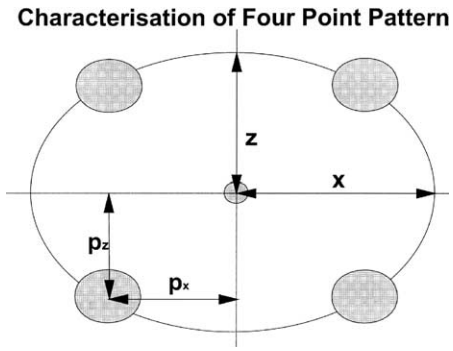

Fig. 14. Characterisation scheme for parameters measured from patterns of Sample B.

scheme, even at the smallest degree of deformation. This indicates that the connectivity of the hard phase is resisting the affine separation of the hard phase domains and that the domains are moving to an alternative mutual arrangement which favours macroscopic yielding and which is linked with the four point diffraction feature. After its initial appearance, the four point feature develops in prominence and changes in shape. A plot of the coordinates of the maximum in intensity is shown in Fig. 16 in terms of the ratio parameters $(p_x/p_{x0})^2$ and p_{z0}/p_z. In this plot, p_{x0} and p_{z0} are the coordinates of the maximum at the initial appearance of the four point pattern in frame 4 at a draw ratio of 1.12. It will be noted that there is a region up to around frame 15 where these two sets of parameters superpose in a linear manner and thereafter tend to diverge. Also shown plotted in this figure is the macroscopic draw ratio. Although the region of linear superposition is displaced from the draw ratio plot, the slope is similar to the macroscopic draw ratio. There is, therefore, an hint here that the rearranged structure that is associated with the four point pattern may be deforming in a systematic way analogous to that observed with Sample A. The four point pattern can be considered as a lattice of higher symmetry which represents the correlations of the hard phase regions after the rearrangement.

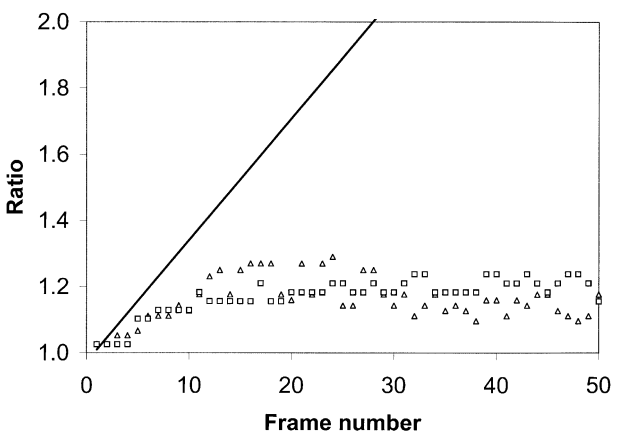

Fig. 15. Plots versus draw ratio for Sample B from ESRF experiment, showing relationship with the affine deformation scheme: $\square = x^2/x_0^2$; $\triangle = z_0/z$; full line = predicted affine behaviour. Each frame corresponds to a time interval of 3.2 s.

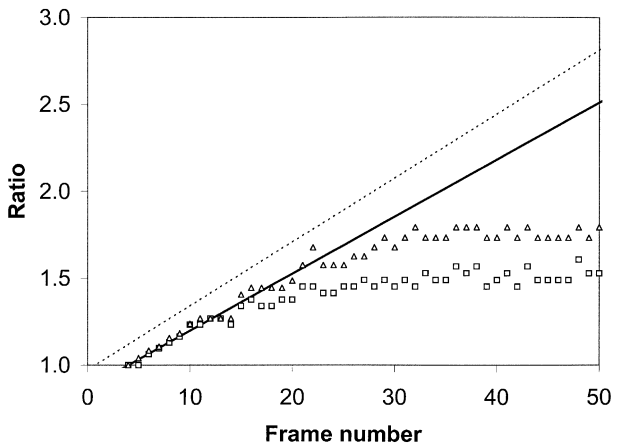

Fig. 16. Plots for Sample B from ESRF experiment of the position of the maxima of the four point patterns in relation to draw ratio and rescaled draw ratio: $\square = px^2/px_0^2$; $\triangle = pz_0/p_z$; dashed line = actual draw ratio; continuous line = rescaled draw ratio. Each frame corresponds to a time interval of 3.2 s.

From the point of view of continuing deformation past the yield, the new arrangement should be considered as a new starting point. Accordingly, one should consider the degree to which subsequent deformation beyond a draw ratio of 1.12 follows an affine scheme. It is therefore more appropriate to compare the $(p_x/p_{x0})^2$ and p_{z0}/p_z parameters with a rescaled draw ratio $= \lambda/1.12$. As shown in Fig. 16, there is then a good agreement between both parameters and the rescaled draw ratio. This shows that the new structural arrangement of the hard phase regions has components that deform affinely in the immediate region beyond the mechanical yield process up to a draw ratio of around 1.4. However, beyond this, there is a trend in the four point pattern to stabilise so that beyond a draw ratio of around 2.0, there is little change in the position of the four point maxima.

4.5. Variations in invariant integral

Samples A and B have been synthesised from the same chemical building blocks. The difference between them is in the length distribution of the blocks. In Sample A there is a near random distribution of blocks whereas in Sample B, both the hard and soft blocks are monodisperse in sequence. If the partition of the hard and soft segments into hard and soft domains had been the same then the invariant integrals for two-phase morphologies would also be expected to be the same, irrespective of actual morphology and would be given by

$$\mathrm{Inv} = \phi(1-\phi)\Delta\rho_e^2 \tag{14}$$

where ϕ is the volume fraction of the hard phase domains, and $\Delta\rho_e$ is the difference in electron density between the hard and soft phases.

The smaller invariant of Sample A which is shown in Table 1 suggests that because of the polydispersity, some of

the hard segments have been incorporated into the soft phase domains thus reducing both ϕ and $\Delta\rho_e$. The extent of the incorporation can be estimated if one assumes that the electron densities of each phase are directly related to the amount of hard and soft segments distributed in each phase. Thus, if the modified volume fraction is ϕ' then it can be shown by simple proportionality that the modified invariant Inv′ will be given by:

$$\frac{\mathrm{Inv}'}{\mathrm{Inv}} = \frac{\phi'}{\phi}\frac{(1-\phi)}{(1-\phi')} \tag{15}$$

On the basis of Eq. (15), the observed reduction of the invariant of Sample A by a factor of 0.73 relative to that of Sample B would infer that the nominal hard phase volume of 0.36 has been reduced to around 0.30 in Sample A. Such a reduction in ϕ could partly explain the lower initial modulus of Sample A.

Several authors have noted that the modulus of such polyurethanes can be reasonably represented by the Davies equation [30–32]

$$G^{1/5} = \phi_A G_A^{1/5} + \phi_B G_B^{1/5} \tag{16}$$

where ϕ_A and G_A are the volume fractions and modulus of phase A and similarly for ϕ_B and G_B.

Davies [33] derived Eq. (16) using a self-consistent field theory to account for two-phase materials where there was a degree of continuity between phases. According to Eq. (16), a reduction in ϕ from 0.36 to 0.3 would reduce the modulus by around 60%, which is comparable with the observed 64% lower modulus in Fig. 3.

A reduction in ϕ would also be expected to reduce the degree of connectivity between hard phase domains. This would be consistent with the difference in deformation behaviour of the phase morphologies. The reduced connectivity in Sample A would facilitate the hard domains moving relatively to each other in an affine way as in the above particulate model. A greater degree of connectivity would provide more resistance, as in Sample B.

The small reduction in the invariant during deformation of Sample A shown in Fig. 7 could also be the result of a reduction in hard phase volume fraction. This would be consistent with the above speculations on the reduction in the fictive parameter z_f which can be interpreted as an elimination of smaller hard phase domains under the influence of higher localised stresses. According to Eq. (15), the observed reduction of invariant would suggest an elimination of 0.02 volume fraction of hard domains. By an analogous reasoning, the small increase in invariant for Sample B shown in Fig. 8 would suggest a growth in hard phase domains by a similar amount. It is therefore a possibility that, when the morphology of Sample B 'stabilises' at high draw ratios, conditions may favour a small degree of accretion of hard segments.

4.6. Implications of analyses

The above analyses of the developing SAXS patterns provide a strong indication of both the manner of deformation of the mesophase morphology and the nature of the initial morphologies themselves. There are clear differences between the two samples which originate from the polydispersity of the hard and soft blocks. The difference in phase volume fractions that is indicated by the invariant of the undeformed states is an important factor, that not only contributes to differences in modulus but also leads to different consequences after yielding.

The lower hard phase volume in Sample A is not unexpected. The polydispersity in the hard block lengths will result in some of the shorter blocks being incorporated in the soft mesophase regions. The resulting lower phase volume will reduce the probability of connectivity between hard domains. This helps to explain why the SAXS patterns of Sample A can so successfully be interpreted via the particulate affine model in which the concentration of hard phase regions can be approximated to particles that separate from each other in an affine manner. The analysis implies that any such connections do not significantly impair the movement of the main hard phase concentration during the initial deformation. This appears to hold even during the mechanical yielding process where it is presumed that any such connections will be broken.

The behaviour of Sample B is indicative of a much more substantial connectivity of the hard phase regions. The connectivity resists the affine separation of the hard phase regions during the yield process and causes the morphology to deform into a more structured arrangement that appears to aid compliance, possibly by involving localised shear of the morphological units. This rearranged structure has a symmetry which effectively forms a crude lattice. After yielding, there is a range of deformation where this lattice itself deforms affinely. The analysis on this level is not able to define the nature of the morphology that is represented by this crude, deforming lattice. One can speculate that the hard phase may at this stage resemble lamellae or a series of localised, linked particles.

Differences between the samples also occurs at higher draw ratios >1.5. In Sample A there is evidence that the main particulate concentrations of hard phase continue to separate in an affine way but with the smaller, less stable domains being eliminated. In Sample B, the crude lattice appears to approach a stabilised arrangement that nonetheless enables considerable extra, uniform extension to occur. One possibility is that this behaviour involves a combination of continuous elimination of hard phase in regions of high local stress and reformation of hard phase in regions of lower stress, such that the overall morphology remains similar.

The above conclusions are broadly in agreement with various interpretations of previous studies [15,17,18].

Further experiments and analyses are now in progress to

determine the degree to which the changes in morphology are dependent on the degree of strain imposed during mechanical cycling.

5. Conclusions

The analysis of the deforming SAXS patterns has not only provided information on the deforming morphology. It has also given additional insight into the nature of the undeformed morphology that could not be anticipated from the isotropic, undeformed SAXS. The two samples exhibit contrasting behaviour which are a consequence of the differences in sequence distribution. Both cases show examples where the main features of the intensity function in reciprocal space undergo an affine deformation consistent with the deformation of the samples in real space.

In Sample A where the sequence lengths are randomised, the affine deformation is consistent with the hard phase domains behaving as particles located on a statistical lattice. The affine deformation of the lattice points occurs from the initial state and continues through the mechanical yield process up to draw ratios ~ 1.25. This implies that any hard phase connectivity, which would be broken down during the yielding, does not impede the affine movement of the hard domains. At high draw ratios there is evidence that the less stable domains are progressively eliminated.

In Sample B where the sequence lengths are monodisperse, the hard phase domains have a more substantial connectivity which prevents initial affine behaviour. The breakdown in the connectivity at yield is associated with a re-organisation of hard domains into a more structured morphology that gives rise to four point maxima in reciprocal space. In this sample, it is the four point feature that deforms in an affine manner consistent with the real space deformation up to draw ratios ~ 1.5. At higher draw ratios there is a trend to an asymptotic arrangement that enables the sample morphology to accommodate the higher strain. It is a possibility that this involves a continuous breakdown and reformation of hard phase regions.

Acknowledgments

We thank Hans Verbeke, Bill Daunch and Jan-Willem Leenslag for making available elastomer samples for this study. We thank Antony Gleeson for support in using beamline 16.1 at the SRS and Urban Voker for providing facilities for obtaining the data from beamline ID2A at the ESRF. This work is supported by EPSRC Grant GR/M/39909.

References

[1] Ryan AJ, Willkomm WR, Bergstrom TB, Macosko CW, Koberstein JT, Yu CC, Russell TP. Macromolecules 1991;24:2883.
[2] Elwell MJ, Mortimer S, Ryan AJ. Macromolecules 1994;27:5428.
[3] Ryan AJ, Macosco CW, Bras W. Macromolecules 1992;25:6277.
[4] Garret JT, Lin JS, Runt J. Macromolecules 2002;35:161.
[5] Ryan AJ, Naylor S, Komanschek B, Bras W, Mant GR, Derbyshire GE. In: Provder T, editor. Hyphenated techniques in polymer characterization. Washington, DC: American Chemical Society; 1994.
[6] Koberstein JT, Stein RS. J Polym Sci, Part B: Polym Phys Ed 1983;21:1439. see also page 2181.
[7] Leung LM, Koberstein JT. J Polym Sci, Part B: Polym Phys Ed 1985;23:1883.
[8] Cooper SL, Tobolsky AV. J Appl Polym Sci 1966;10:1837.
[9] Estes GM, Cooper SL, Tobolsky AV. J Macromol Sci, Rev Macromol Chem 1970;4:167.
[10] Seymour RW, Cooper SL. Macromolecules 1973;6:48.
[11] Huh SD, Cooper SL. Polym Engng Sci 1971;11:369.
[12] Bonart R. J Macromol Sci, Phys 1968;2:115.
[13] Bonart R, Morbitzer L, Hentze G. J Macromol Sci, Phys 1969;3:337.
[14] Desper CR, Schneider NS, Jasinski JP, Lin JS. Macromolecules 1985;18:2755.
[15] Moreland JC, Wilkes GL. J Appl Polym Sci 1991;43:801.
[16] Eisenbach CD, Baumgartner M, Gunter C. Polym Prepr (Am Chem Soc, Div Polym Chem) 1985;26:7.
[17] Eisenbach CD, Ribbe A, Gunter C. Macromol Rapid Commun 1993;15:395.
[18] Musselman SG, Santosussu TM, Barnes JD, Sperling LH. J Polym Sci, Part B: Polym Phys 1999;37:2586.
[19] Peebles LH. Macromolecules 1976;9:58.
[20] Blundell DJ, Martin C, Mahendrasingam A, Fuller W, Eeckhaut G. Fibre Diffract Rev 2002; in press.
[21] Balta-Callega FJ, Vonk CG. X-ray scattering of synthetic polymers. Amsterdam: Elsevier; 1989.
[22] Ruland W. J Appl Crystallogr 1971;4:70.
[23] Russel TP, Lin JS, Spooner S, Wignall GD. J Appl Crystallogr 1988;21:629.
[24] Porod G. In: Glatter O, Kratky O, editors. Small angle X-ray scattering. London: Academic Press; 1982.
[25] Mahendrasingam A, Fuller W, Forsyth VT, Oldman RJ, Mackerron DH, Blundell DJ. Rev Sci Instrum 1992;63:1087.
[26] Hughes DJ, Mahendrasingam A, Martin C, Oatway WB, Heeley EL, Bingham SJ, Fuller W. Rev Sci Instrum 1999;70:4051.
[27] Zernike F, Prins JA. Z Phys 1927;41:184.
[28] Rayleigh Lord. Proc R Soc (Lond) 1911;A84:25.
[29] Guinier A. X-ray diffraction in crystals, imperfect crystals and amorphous bodies. San Francisco: Freeman; 1963.
[30] Stanford JL. In: Stepto RFT, editor. Polymer networks. New York: Wiley; 1980. chapter 5.
[31] Stanford JL, Wilkinson AN, Lee DK, Ryan AJ. Plast, Rubber Process Appl 1990;13:111.
[32] Klein PG, Ebdon JR, Hourston DJ. Polymer 1988;29:1079.
[33] Davies WEA. J Phys D: Appl Phys 1971;4:318.